Unraveling the structure-activity-selectivity relationships in furfuryl alcohol photoreforming to H_2 and hydrofuroin over $Zn_xIn_2S_{3+x}$ photocatalysts

Denny Gunawan [a], Jodie A. Yuwono [a,b], Priyank V. Kumar [a], Akasha Kaleem [c], Michael P. Nielsen [c], Murad J.Y. Tayebjee [c], Louis Oppong-Antwi [d], Haotian Wen [d], Inga Kuschnerus [e], Shery L.Y. Chang [d,e], Yu Wang [f], Rosalie K. Hocking [g], Ting-Shan Chan [h], Cui Ying Toe [a,i,*], Jason Scott [a,*], Rose Amal [a,*]

[a] School of Chemical Engineering, The University of New South Wales, Sydney, NSW 2052, Australia
[b] College of Engineering and Computer Science, Australian National University, ACT 2601, Australia
[c] School of Photovoltaic and Renewable Energy Engineering, The University of New South Wales, Sydney, NSW 2052, Australia
[d] School of Materials Science and Engineering, The University of New South Wales, Sydney, NSW 2052, Australia
[e] Electron Microscope Unit, Mark Wainwright Analytical Centre, The University of New South Wales, Sydney, NSW 2052, Australia
[f] Solid State and Elemental Analysis Unit, Mark Wainwright Analytical Centre, The University of New South Wales, Sydney, NSW 2052, Australia
[g] Department of Chemistry and Biotechnology, School of Science, Technology and Engineering, Swinburne University of Technology, Melbourne, VIC 3122, Australia
[h] National Synchrotron Radiation Research Center, Hsinchu 30076, Taiwan
[i] School of Engineering, The University of Newcastle, Callaghan, NSW 2308, Australia

ARTICLE INFO

ABSTRACT

$Zn_xIn_2S_{3+x}$ has emerged as a promising candidate for alcohol photoreforming based on C-H activation and C-C coupling. However, the underlying structure-activity-selectivity relationships remain unclear. Here we report on $Zn_xIn_2S_{3+x}$ with varying Zn:In:S ratios for visible-light-driven furfuryl alcohol reforming into H_2 and hydrofuroin, a jet fuel precursor, via C-H activation and C-C coupling. $S^{\bullet}$ radicals are directly identified as the catalytically active sites responsible for C-H activation in furfuryl alcohol, promoting selectivity toward H_2 and hydrofuroin. The optimum $Zn_xIn_2S_{3+x}$ activity derives from a trade-off between enhanced carrier dynamics and diminished visible light absorption as the x value in $Zn_xIn_2S_{3+x}$ increases. Further, a higher Zn-S:In-S layer ratio prolongs the $S^{\bullet}$ lifetime in the Zn-S layer, promoting C-H activation and delivering a higher C-C coupling product selectivity. The findings represent a step toward further establishing sulfide-based photocatalysts for sustainable H_2 production via organic photoreforming.

1. Introduction

As the world races to meet its emission targets via decarbonization, H_2 has gained significant attention as a clean fuel and industrial feedstock [1,2]. Consequently, developing affordable and environmentally benign H_2 production technologies is now an intense subject of research. Solar-driven water splitting over semiconductor photocatalysts has been extensively investigated as an attractive route for H_2 generation [3]. However, the sluggish O_2 evolution reaction results in an inferior solar-to-H_2 energy conversion efficiency. Photoreforming, which replaces the O_2 evolution reaction with more thermodynamically favorable organic oxidation, has been demonstrated to appreciably accelerate the H_2 evolution rate [4]. Additionally, photoreforming has the potential to simultaneously produce H_2 using the photogenerated electrons and valuable chemicals or fuels using the holes [5,6]. This could assist with alleviating global reliance on fossil carbon sources and decreasing the cost of solar H_2.

Waste biomass is a compelling substrate for photoreforming due to its abundance and high annual yield from various sectors including agricultural, municipal, and industrial [6,7]. Utilizing waste biomass for H_2 generation can significantly contribute to low-cost renewable energy production while simultaneously addressing environmental issues [8,9].

---

* Corresponding authors at: School of Chemical Engineering, The University of New South Wales, Sydney, NSW 2052, Australia.
E-mail addresses: cuiying.toe@newcastle.edu.au (C.Y. Toe), jason.scott@unsw.edu.au (J. Scott), r.amal@unsw.edu.au (R. Amal).

In this context, furfuryl alcohol (FOL) is an attractive organic precursor for industrially important chemicals and fuels which can be obtained from decarbonylation of lignocellulose-derived 5-(hydroxymethyl) furfural (HMF) [10–12]. Han et al., for instance, have demonstrated a visible-light-driven conversion of FOL to H_2 and furfural or furoic acid on a Ni/CdS photocatalyst [13].

Photoreforming typically converts alcohols into H_2 and their corresponding carbonyl compounds via O-H activation followed by C-H activation or vice versa [14,15]. C-H activation of organic molecules followed by C-C coupling to form longer-chain carbon products via photoreforming has recently received considerable attention. The approach has enabled direct synthesis of ethylene glycol from methanol [16,17], 2,3-butanediol from ethanol [17], hydrobenzoin, benzoin, and deoxybenzoin from benzyl alcohol [18–20], and diesel precursors from 2-methylfuran or 2,5-dimethylfuran [21]. Through C-H activation and C-C coupling, FOL can be simultaneously converted to H_2 and hydrofuroin (HF, a known jet fuel precursor). The HF may then be subjected to hydrodeoxygenation (HDO) to yield C_{10} alkanes that can serve as a drop-in sustainable aviation fuel (Fig. 1) [22].

C-H activation is considered one of the greatest challenges in catalysis due to the relatively inert nature of the sp^3 C-H bond. In the presence of more reactive functional groups, such as the hydroxyl group (-OH) in alcohols, selective α-C-H activation to form a carbon-centered radical is even more challenging [23,24]. Typically, C-H activation is more kinetically challenging than O-H activation due to the more unstable transition state in C-H cleavage than that in O-H cleavage via a stepwise proton transfer followed by an electron transfer (PT-ET) mechanism (Eq. 1) [16,25,26].

$$X - H \xrightarrow{-H^+} X^- \xrightarrow{-e^-} X^{\cdot} \qquad (1)$$

Xie et al., for instance, compared the activation energy barriers for α-C-H activation and O-H activation of methanol on rutile $TiO_2(110)$ via the PT-ET mechanism [16]. The energy barrier to afford the α-C-H activation transition state ($^{\cdot}CH_2OH$) was 1.4 eV higher than for the O-H activation transition state (CH_3O^-). Nevertheless, preferential C-H activation over O-H activation may occur on photocatalysts that can avoid the formation of unstable C-H activation transition state by facilitating a

concerted proton-electron transfer (CPET) mechanism (Eq. 2) [16].

$$X - H \xrightarrow{-H^{\cdot}} X^{\cdot} \qquad (2)$$

For example, the calculated activation energy barrier for α-C-H activation of methanol on CdS(100) via the CPET mechanism was 0.5 eV lower than for O-H activation, leading to more selective α-C-H activation of methanol [16]. Following C-H activation step, the generated carbon-centered radical must be rapidly desorbed from the photocatalyst surface to progress to the C-C coupling reaction [27–29]. Otherwise, the carbon-centered radical may be further oxidized to an aldehyde, ketone, or carboxylic acid and subsequently CO or CO_2. Designing semiconductor photocatalysts with suitable active sites and properties is crucial to achieve the preferential C-H activation and C-C coupling of bio-alcohols.

$Zn_xIn_2S_{3+x}$ is an attractive class of ternary metal sulfide photocatalysts used for numerous organic synthesis reactions. In addition to the excellent visible light response and lower toxicity compared to CdS, the band structures of $Zn_xIn_2S_{3+x}$ are simple to engineer by varying the Zn:In:S ratio or doping with other metals. For example, Zhang et al. demonstrated that $Zn_2In_2S_5$ delivered an improved H_2 evolution rate and higher C-C coupling product selectivity compared to $ZnIn_2S_4$ and $Zn_3In_2S_6$ during methanol and ethanol photoreforming [17]. Furthermore, a tandem redox of benzyl alcohol to deoxybenzoin and H_2 was reported over $Zn_xIn_2S_{3+x}$ (with a Zn:In ratio ≥ 0.2) due to the more reductive conduction band (CB) [20]. Beyond tuning the stoichiometric ratio, doping Ru into $ZnIn_2S_4$ was found to invoke dehydrogenative C-C coupling of methylfurans due to an improved charge separation [21]. Recently, a suite of challenging organic reactions, such as the coupling of phenylacetylene and benzyl mercaptan on $ZnIn_2S_4$ [30], pinacol coupling of benzaldehyde and furfural on $ZnIn_2S_4$ [31], and β-O-4 bond cleavage of lignin model compounds on $Zn_xIn_2S_{3+x}$ [32], has also been reported. The photocatalytic activity and selectivity of $Zn_xIn_2S_{3+x}$ has been shown as tunable by regulating the stoichiometric composition, rendering $Zn_xIn_2S_{3+x}$ as a potential photocatalyst for more efficient photoreforming via the C-H activation and C-C coupling pathway.

Here we report on the design of $Zn_xIn_2S_{3+x}$ photocatalysts where the Zn:In:S ratio is tuned to regulate visible-light-driven FOL reforming
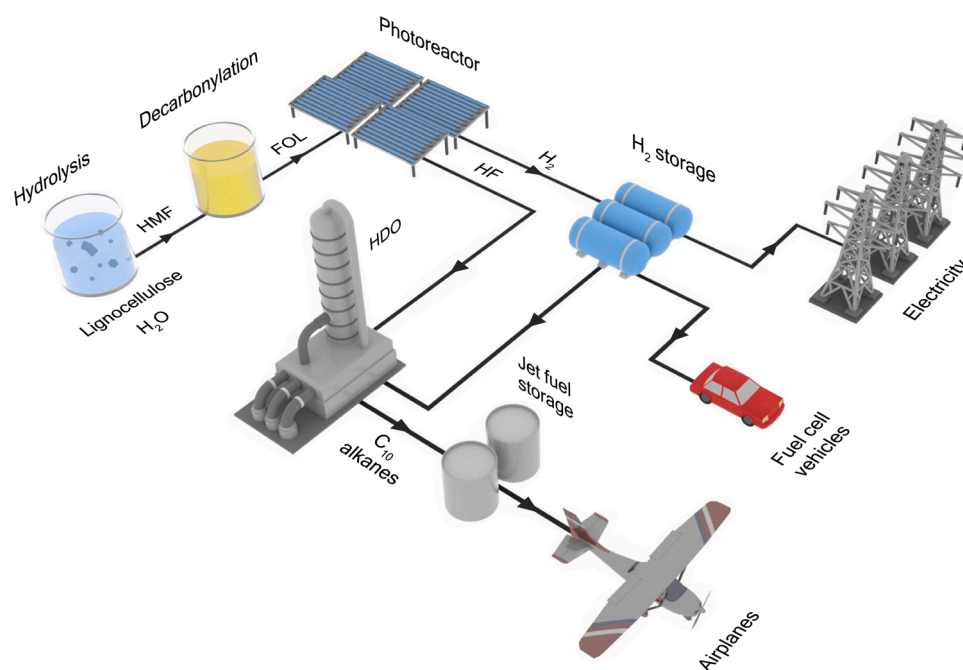
Fig. 1. Conceptual process flow diagram for the coproduction of H_2 and sustainable jet fuel from lignocellulosic waste. Furfuryl alcohol (FOL) is obtained by the decarbonylation of lignocellulose-derived 5-(hydroxymethyl)furfural (HMF) and photoreformed into H_2 and hydrofuroin (HF, a known jet fuel precursor). HF is separated and converted to C_{10} alkanes via hydrodeoxygenation (HDO).

based on the C-H activation and C-C coupling pathway to produce H_2 and hydrofuroin (a jet fuel precursor). The malleable nature of $Zn_xIn_2S_{3+x}$ is used to control its physicochemical and electronic characteristics and unravel the underlying and elusive structure-activity-selectivity relationships for the C-H activation and C-C coupling pathway. On varying the stoichiometric Zn:In:S ratio in $Zn_xIn_2S_{3+x}$, the crystal and electronic band structures as well as the sulfur speciation are altered, in turn defining the photocatalytic activity and selectivity. Fresh insights on the reaction mechanism are provided with direct evidence on the catalytically active sites offered for the first time. Finally, the active site lifetime is identified as an activity-selectivity descriptor for the C-H activation and C-C coupling pathway. The findings illustrate the significant potential in engineering photocatalyst structures for controlling process activity and selectivity during photoreforming to produce green H_2 and value-added chemicals.

2. Experimental

2.1. Chemicals

Zinc acetate dihydrate ($Zn(CH_3COO)_2 \cdot 2\ H_2O$, $\geq 98\%$), indium(III) chloride tetrahydrate ($InCl_3 \cdot 4\ H_2O$, 97%), thioacetamide (98%), and furfuryl alcohol (98%). All chemicals were used as received.

2.2. Photocatalyst synthesis

$Zn_xIn_2S_{3+x}$ ($x = 1$–4) photocatalysts were synthesized by a low-temperature wet chemical approach. In brief, $1.2x$ mmol of Zn ($CH_3COO)_2 \cdot 2\ H_2O$, 2.4 mmol of $InCl_3 \cdot 4\ H_2O$, and $(7.2 + 2.4x)$ mmol of thioacetamide were dissolved in 200 mL of Milli-Q water and heated in an oil bath at 95 °C for 5 h under vigorous stirring. The mixture was then cooled to room temperature and sonicated for 1 h. The precipitate was collected by centrifuging, washed with absolute ethanol and Milli-Q water multiple times, and vacuum dried at 60 °C.

2.3. Photocatalyst characterization

Powder X-ray diffraction (XRD) patterns were collected on a PANalytical Aeris diffractometer using Cu Kα radiation at 40 kV and 15 mA. Pair distribution function (PDF) analysis was employed to determine the phase. The measurements were conducted using an Empyrean diffractometer (Malvern PANalytical, Netherlands) with Ag X-ray source ($\lambda = 0.559$ Å) and Galipix detector. The power setting was 60 kV and 30 mA, capillary tube mode, the scan range from 1.2° to 138° (2θ) and step size 0.014° (2θ). The data analysis and simulation used PDFgui software [33]. High-resolution transmission electron microscopy (HR-TEM) and energy dispersive spectroscopy (EDS) mapping were conducted on a JEOL JEM-F200 microscope operating at 200 kV. High-resolution annular dark field scanning transmission electron microscopy (HR-ADF-STEM) was conducted using an aberration-corrected JEOL GrandArm300F2 operating at 80 kV. Scanning electron microscopy (SEM) images were obtained on a FEI Nova NanoSEM 450 microscope. Atomic composition of the samples was determined on a PerkinElmer OPTIMA 7300 inductively coupled plasma atomic emission spectrometer (ICP-AES) after aqua regia digestion. The specific surface areas were measured on a Micromeritics TriStar 3030 using the N_2 physisorption method at -195.8 °C. Prior to analysis, samples were degassed at 150 °C for 3 h under vacuum.

UV–vis diffuse reflectance spectroscopy (DRS) was performed on a Shimadzu UV-3600 UV–vis–NIR spectrophotometer with $BaSO_4$ as the reference and analyzed using Kubelka-Munk model. Steady-state photoluminescence (PL) spectra of the samples in water (250 mg L^{-1}) were measured on a HORIBA FluoroMax-4 spectrofluorometer with 350 nm laser excitation.

X-ray photoelectron spectroscopy (XPS) and valence band XPS (VB XPS) were performed on a Thermo Scientific ESCALAB 250Xi instrument

with Al Kα radiation source. X-ray absorption spectroscopy (XAS) measurements were collected on beamline TLS-16A1 at the National Synchrotron Radiation Research Center (NSRRC), Hsinchu, Taiwan operated at 1.5 GeV with a current of 360 mA. All spectra were recorded in fluorescence yield (FY) mode at room temperature using a Lytle detector.

Photoelectrochemical measurements were conducted on an Autolab potentiostat PGSTAT204 using a standard three-electrode cell with a working electrode, Pt plate counter electrode, and an Ag/AgCl reference electrode. A 0.5 M Na_2SO_4 aqueous solution was used as the electrolyte. The working electrode was prepared on FTO glass. The photocatalyst was dispersed in ethanol using ultrasonication with the suspension then added dropwise directly onto the FTO. The film was vacuum-dried at 60 °C. The photocatalyst density was 2 mg cm^{-2}. The light source was an Oriel solar simulator. Transient photocurrent responses were acquired under an applied potential of 1.0 V vs RHE. Electrochemical impedance spectroscopy was conducted under an applied potential of -0.6 V vs RHE and frequency from 0.01 Hz to 1000 kHz. Mott-Schottky measurements were performed across a potential range of -0.2–1.2 V vs RHE and frequency of 1000 Hz.

2.4. Photoreforming experiments

Photoreforming reactions were conducted in a spiral photoreactor as described elsewhere, with some modifications [34], connected to an online gas chromatograph (GC). Typically, 100 mg of photocatalyst was dispersed in 100 mL of 10 mM aqueous furfuryl alcohol solution under sonication. The mixture was then added to, and circulated around, the photoreactor. Prior to irradiation, the photoreactor was purged with N_2. All experiments were performed under illumination by blue light-emitting diodes (LEDs, $\lambda = 420$ nm, I = 15 mW cm^{-2}) as the visible light source or a NEC blacklight fluorescent tube (FL20SBL, I = 5 mW cm^{-2}) as the UV source.

2.5. Product analysis

H_2 and other gas components (CO and CO_2) were quantitatively analyzed by an online Shimadzu GC-2014 equipped with a thermal conductivity detector (TCD) and flame ionization detector (FID). Ar was used as the carrier gas with a column temperature of 70 °C. Gas samples from the photoreactor headspace were automatically collected every 1 h for analysis. Furfuryl alcohol, furfural, and hydrofuroin in the liquid phase were quantified using nuclear magnetic resonance (NMR) spectroscopy (Bruker Avance III 600 MHz NMR). After a defined reaction time, the liquid samples were withdrawn from the photoreactor, filtered through a 0.22 μm nylon syringe filter, mixed with D_2O (volume ratio of sample to D_2O was 9:1) and sodium acetate as the internal standard, and then analyzed by ^1H NMR spectroscopy using a presaturation technique for water suppression.

Liquid chromatography-mass spectrometry (LC-MS) was employed to analyze the furanic oligomers. In brief, the photocatalyst suspension following reaction was collected and furanic species extracted using chloroform. After separation, the chloroform extract was analyzed using Q-Exactive HF mass spectrometer with U3000 UHPLC system (ThermoFisher Scientific).

The conversion, yield, selectivity, and carbon balance were calculated as mole percent using Eqs. 3–6, respectively.

$$Conversion\ (mol\%) = \left(1 - \frac{n(Feedstock\ after\ reaction)}{n(Feedstock\ before\ reaction)}\right) \times 100\% \quad (3)$$

$$Yield\ (mol\%) = \frac{n(Product)}{n(Theoretical\ product)} \times 100\% \quad (4)$$

$$Selectivity\ (mol\%) = \frac{Yield\ (mol\%)}{Conversion\ (mol\%)} \times 100\% \quad (5)$$

$$Carbon\ balance\ (mol\%) = \frac{\Sigma n(Product) + n(Feedstock\ after\ reaction)}{n(Feedstock\ before\ reaction)}$$
$$\times 100\% \qquad (6)$$

2.6. Carbon-centered radical detection

An in situ spin radical-trapping technique was carried out to probe the presence of carbon-centered radicals. A 40 mg of $Zn_xIn_2S_{3+x}$ was ultrasonically dispersed in 20 mL of aqueous solution containing 0.4 mmol of 5,5-dimethyl-1-pyrroline N-oxide (DMPO) and 0.4 mmol of furfuryl alcohol (FOL). The resulting mixture was purged with N_2 and illuminated using a UV light-emitting diodes (LEDs, $\lambda = 365$ nm, I $=$ 107 mW cm^{-2}) for 5 h. After the reaction, the supernatant was collected by filtering the suspension through a 0.22 μm nylon syringe filter. The presence of carbon-centered radicals in the supernatant was then examined on an electron paramagnetic resonance (EPR) spectrometer (Bruker EMX) using a capillary tube. The spectrometer was operated at a microwave frequency of 9.84 GHz with a power of 0.63 mW. The supernatant was also analyzed by LC-MS on a Q-Exactive HF mass spectrometer with U3000 UHPLC system (ThermoFisher Scientific).

2.7. Transient absorption spectroscopy

The excited state dynamics of $Zn_xIn_2S_{3+x}$ were measured using a commercial transient absorption spectrometer (Ultrafast Systems, Helios). The spectra were obtained in the visible light region using an optical delay line that measures up to 8 ns with a minimum step size of 14 fs. An amplified laser Ti:Sapphire laser system (Spectra Physics, Solstice ACE) generates ultrashort pulses with wavelength of 800 nm and typical duration of 100 fs at a frequency repetition rate of 1 kHz. The 800 nm pulse, after passing through optical delay stage, was focused on a

sapphire crystal to create a white light supercontinuum covering a 400–780 nm range. Pump pulses (350 nm, FWHM 100 fs, 500 Hz, 25 μJ cm^{-2}) were generated by a TOPAS PRIME optical parametric amplifier (Light Conversion) and used to excite the samples through overlapping the pump and probe pulses at a ~15:1 spot size ratio. The samples were kept at room temperature and spectra were acquired with a 0.581 nm interval and 2 s averaging time.

2.8. Density functional theory (DFT) calculations

DFT calculations were implemented using the Vienna ab-initio simulation package (VASP) [35,36] with the core and valence electronic interactions modelled using the projector augmented wave (PAW) method [37,38]. The Perdew-Burke-Ernzerhof (PBE) exchange-correlation functional [39] was employed. The wavefunctions were expanded with a kinetic energy cut-off of 500 eV and Monkhorst-Pack k-points of $5 \times 5 \times 1$ were used. Geometrical optimizations were achieved by relaxing all ionic positions and supercell vectors until the Hellman-Feynmann forces were less than 0.01 eV Å^{-1}. A vacuum region of 20 Å was introduced in the direction of the z-axis to avoid interactions between periodic images. The dispersion correction was also considered using DFT-D3 method [40].

3. Results and discussion

3.1. Structural characterization

A series of ternary $Zn_xIn_2S_{3+x}$ ($x = 1$–4) photocatalysts were prepared by tuning the concentrations of $Zn(CH_3COO)_2 \cdot 2\ H_2O$, $InCl_3 \cdot 4H_2O$, and thioacetamide precursors. Inductively coupled plasma-atomic emission spectroscopy (ICP-AES) indicates the empirical formulas of the $Zn_xIn_2S_{3+x}$ samples are close to the nominal compositions
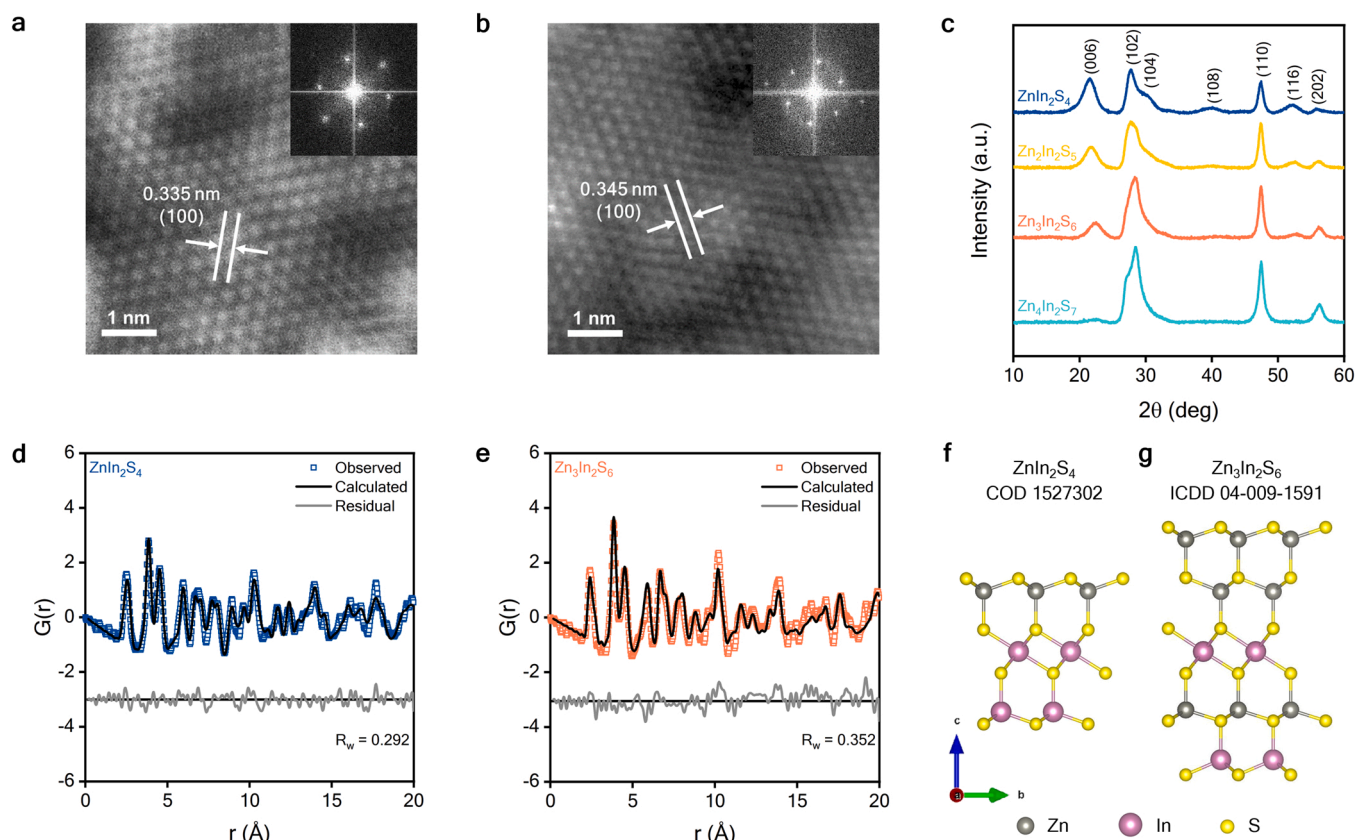
Fig. 2. Physical characteristics of $Zn_xIn_2S_{3+x}$. HR-ADF-STEM images of (a) $ZnIn_2S_4$ and (b) $Zn_3In_2S_6$. Insets: corresponding FFT micrographs. (c) XRD patterns. PDF fitting for (d) $ZnIn_2S_4$ and (e) $Zn_3In_2S_6$. Postulated crystal structures of (f) $ZnIn_2S_4$ and (g) $Zn_3In_2S_6$.

(Table S1). Fig. 2a,b provides high-resolution annular dark field scanning transmission electron microscopy (HR-ADF-STEM) images for the $ZnIn_2S_4$ and $Zn_3In_2S_6$ samples, viewed along the [001] orientation of $Zn_xIn_2S_{3+x}$. The two samples represent the lower and higher x-value materials, respectively. They exhibit similar lattice spacings (0.335 ± 0.003 nm for $ZnIn_2S_4$ and 0.345 ± 0.004 for $Zn_3In_2S_6$), attributed to the interlayer distance d_{100} [41,42] as shown from the electron diffraction simulation in Fig. S1. Similarly, the $Zn_2In_2S_5$ and $Zn_4In_2S_7$ samples have lattice fringes of 0.338 ± 0.002 nm and hexagonal crystal structures as indicated by the respective HR-TEM images and FFT patterns (Fig. S2a,b). The lattice spacings were determined by performing line intensity analysis of the FFT micrographs across three different directions and are reported as the average (Fig. S3a-d). Universally, the findings indicate $Zn_xIn_2S_{3+x}$ materials with x values between 1 and 4 possess nearly identical projections of the hexagonal lattice in the a-b plane.

The X-ray diffraction (XRD) patterns for $Zn_xIn_2S_{3+x}$ (Fig. 2c) show diffraction peaks corresponding to a hexagonal wurtzite crystal phase, confirming the TEM observations. There exist several dissimilarities among the diffraction patterns, indicating subtle variations exist within the $Zn_xIn_2S_{3+x}$ bulk crystal structures beyond the indistinguishable hexagonal lattice (a-b projection). With increasing x, a shift in the (006) peak to a higher angle is apparent, arising from the smaller ionic radius

of Zn^{2+} (0.74 Å) compared to In^{3+} (0.76 Å) [43,44]. Further, the intensity of selected diffraction peaks is varied. The distinct diffraction features among $Zn_xIn_2S_{3+x}$ are ascribed to structural changes in the c direction upon altering the Zn:In:S ratio. To understand the $Zn_xIn_2S_{3+x}$ structural differences, pair distribution function (PDF) analysis was performed. As illustrated in Fig. 2d,e, the PDFs for $ZnIn_2S_4$ and $Zn_3In_2S_6$ are best described by the structures presented in Fig. 2f,g with reasonable fitting agreement factors (R_w) of 0.292 and 0.352, respectively. PDF analyses for $Zn_2In_2S_5$ and $Zn_4In_2S_7$ are provided in Fig. S4a,b with the corresponding crystal structures in Fig. S4c,d. The postulated structures indicate the Zn^{2+} ions are located at the tetrahedral sites (Zn_t) and the In^{3+} ions hosted in the distorted tetrahedral (In_t) and octahedral (In_o) sites [45,46]. The $Zn_xIn_2S_{3+x}$ structures comprise -S-Zn_t-S- units (i.e., Zn-S layer) as well as -S-In_o-S- and -S-In_t-S- units (i.e., In-S layer) where the Zn-S:In-S layer ratio is defined by the x value. For example, the Zn-S: In-S layer ratio in $ZnIn_2S_4$ ($x = 1$) is 1:2 (Fig. 2f), while for $Zn_3In_2S_6$ ($x = 3$) it is 3:2 (Fig. 2g).

The scanning electron microscopy (SEM) images illustrate the differences in $Zn_xIn_2S_{3+x}$ morphology (Fig. S5a-d). $ZnIn_2S_4$ comprises numerous nanosheets, agreeing with the lamellar hexagonal $ZnIn_2S_4$ crystal features. $Zn_2In_2S_5$ and $Zn_3In_2S_6$ exhibit similar sheet-like structures with larger sheets, arising from the increased number of Zn-S layers. When $x = 4$, the shape is partially distorted due to the overly
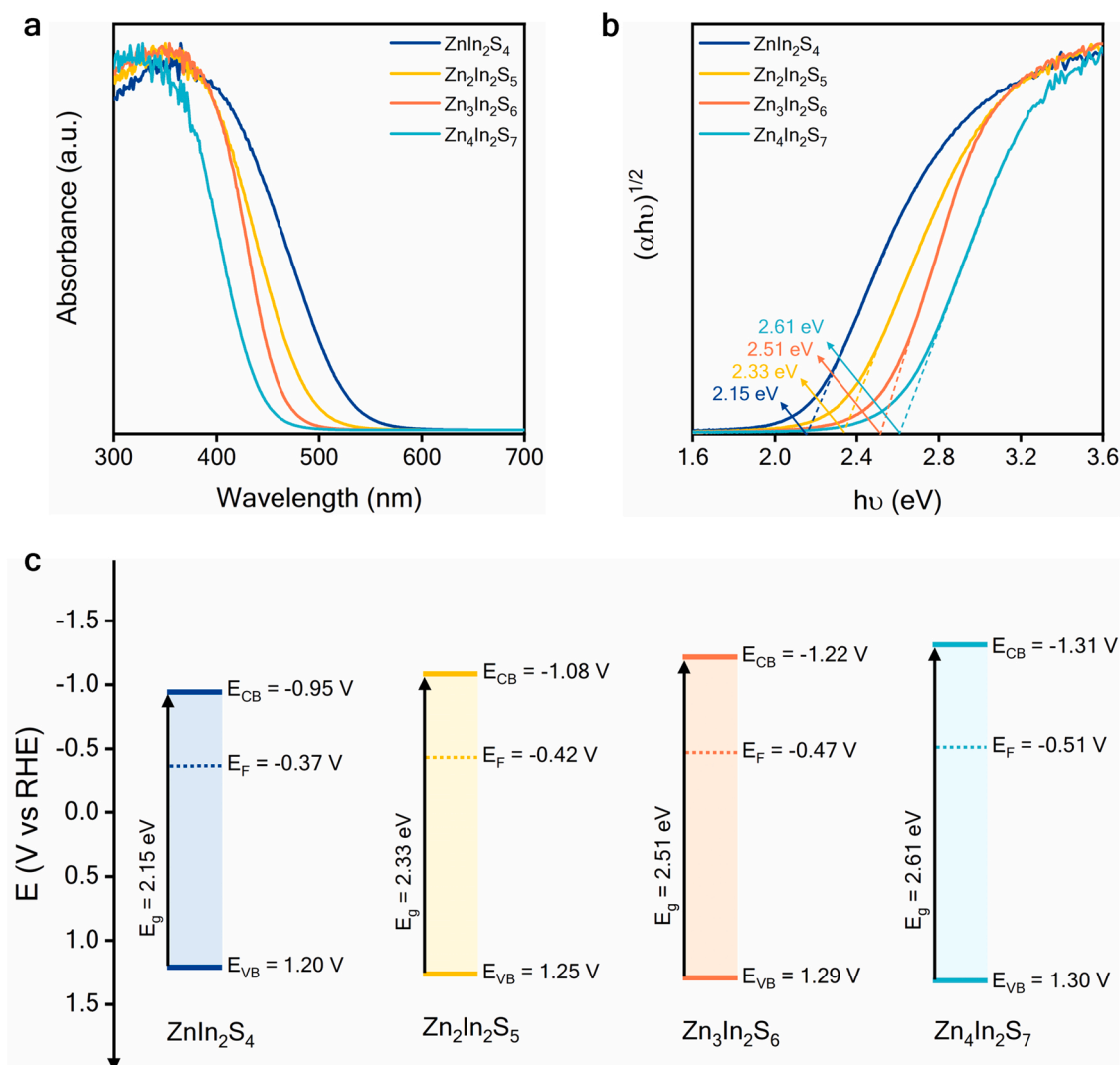
Fig. 3. Electronic band structures of $Zn_xIn_2S_{3+x}$. (a) UV–vis DRS spectra. (b) Calculated Tauc plots (obtained from Kubelka-Munk modelling). (c) Postulated electronic band structures.

large sheets in the structure. The changing $Zn_xIn_2S_{3+x}$ morphologies increase the specific surface area (from 77.8 to 192.3 m^2 g^{-1}, for $x = 1$ and $x = 4$, respectively (Table S2), implying that a higher x value may expose more surficial active sites.

The impact of altering the x value in $Zn_xIn_2S_{3+x}$ on the band structure was studied by UV–vis diffuse reflectance spectroscopy (DRS), electrochemical Mott-Schottky analysis, and valence band X-ray photoelectron spectroscopy (VB XPS). The UV–vis spectra for $Zn_xIn_2S_{3+x}$ (Fig. 3a) show that the light absorption edge shifts to shorter wavelengths with increasing x. The band gap energies, (E_g; evaluated using the Tauc plots from Kubelka-Munk modelling), are 2.15, 2.33, 2.51, and 2.61 eV for $ZnIn_2S_4$, $Zn_2In_2S_5$, $Zn_3In_2S_6$, and $Zn_4In_2S_7$, respectively (Fig. 3b). VB XPS illustrates the energy difference between the Fermi level (E_F) and valence band (E_{VB}) [15,47] is 1.57, 1.67, 1.76, and 1.81 eV for $ZnIn_2S_4$, $Zn_2In_2S_5$, $Zn_3In_2S_6$, and $Zn_4In_2S_7$, respectively (Fig. S6). Mott-Schottky analysis indicates the flat band potentials (vs RHE) are -0.37, -0.42, -0.47, and -0.51 V, respectively (Fig. S7). All $Zn_xIn_2S_{3+x}$ samples exhibit typical n-type semiconductor characteristics, affirmed by the positive Mott-Schottky slopes [48]. Generally, the flat band potential of an n-type semiconductor is close to its Fermi level [48]. Compiling the findings, the postulated band structures of each $Zn_xIn_2S_{3+x}$ sample are illustrated in Fig. 3c. The diagrams show that the $Zn_xIn_2S_{3+x}$ E_{VB} slightly shift to more positive values with increasing x. The shift derives from the VB of $Zn_xIn_2S_{3+x}$ comprising hybrid S 3p and Zn 3d orbitals while the In 5 s orbital is located at more negative energy level and does not contribute significantly to the VB [45]. Consequently, increasing the x value invokes a small shift toward the Zn 3d orbital level which has more positive energy value. In contrast, the E_{CB} shift significantly to more negative values. The CB of $Zn_xIn_2S_{3+x}$ comprises In 5 s and 5p orbitals mixed with Zn 4 s and 4p orbitals [45]. Increasing the x value shifts the CB toward the Zn 4 s and 4p orbitals that are located at more negative potentials compared to In 5 s and 5p.

3.2. Furfuryl alcohol photoreforming

The $Zn_xIn_2S_{3+x}$ materials were assessed for aqueous FOL photoreforming under visible light irradiation ($\lambda = 420$ nm). Upon illumination, the photogenerated electrons reduce protons to H_2 while the holes oxidize the FOL. Fig. 4a displays the time-dependent H_2 evolution profiles for $Zn_xIn_2S_{3+x}$. Increasing x from 1 to 3 improves the H_2 yield over 5 h of illumination from 1.17 mmol g^{-1} ($ZnIn_2S_4$) to 2.92 mmol g^{-1} ($Zn_3In_2S_6$). Increasing x to 4 ($Zn_4In_2S_7$) lowers the H_2 yield (2.37 mmol g^{-1}) over 5 h of illumination. Simultaneously, the

$Zn_xIn_2S_{3+x}$ photocatalysts produce HF and furfural (FAL) as the two primary products (Fig. 4b). Table S3 summarizes the conversion, yield, and selectivity in mole percent for $Zn_xIn_2S_{3+x}$ photocatalysts under visible light. HF and FAL yields by $ZnIn_2S_4$ ($x = 1$) after 5 h of reaction are 0.54 and 0.70 mmol g^{-1}, respectively, corresponding to 32.3% HF selectivity and 21.2% FAL selectivity. Increasing x from 1 to 2 invokes HF and FAL yields of 1.05 and 0.68 mmol g^{-1}, respectively, with a higher HF selectivity (40.1%) and lower FAL selectivity (13.0%). $Zn_3In_2S_6$, which offered the best H_2 productivity, gives HF and FAL yields of 1.13 and 0.74 mmol g^{-1}, respectively, with a higher HF selectivity (43.7%) and similar FAL selectivity (13.5%). Mirroring the H_2 production rate, $Zn_4In_2S_7$ generated less HF and FAL (0.99 and 0.56 mmol g^{-1}, respectively) compared to $Zn_3In_2S_6$, while HF selectivity was similar (43.3%) and FAL selectivity slightly lower (12.2%). The diminished activity between $Zn_3In_2S_6$ to $Zn_4In_2S_7$ is attributed to the wider band gap of $Zn_4In_2S_7$ leading to poorer visible light absorption (particularly at 420 nm (Fig. 3a) which is the blue light diode wavelength). The result was validated by conducting the photoreforming under UV irradiation (Fig. S8a,b), showing higher activity for $Zn_4In_2S_7$ than $Zn_3In_2S_6$.

Carbon balance calculations were then undertaken for furfuryl alcohol photoreforming under visible light irradiation on $ZnIn_2S_4$, $Zn_2In_2S_5$, $Zn_3In_2S_6$, and $Zn_4In_2S_7$. The carbon balance percentages for $ZnIn_2S_4$, $Zn_2In_2S_5$, $Zn_3In_2S_6$, and $Zn_4In_2S_7$ were 83.8%, 73.1%, 72.0%, and 76.8%, respectively (Table S3). This indicates that unknown byproducts may be formed in the gas and/or solid phases. As gaseous carbon species including CO_2 and CO were observed to be negligible, the byproducts are likely to be high molecular mass species insoluble in water and deposited on the photocatalyst surface. This hypothesis was evidenced by a significant increase in the carbon atomic percentage on the post-reaction photocatalyst surfaces, observed from C 1 s XPS analysis, from 12.72 at% to 33.57 at% (Fig. S9). In addition, the ATR-IR spectrum of spent $Zn_3In_2S_6$ shows that the carbon species left on the surface has furanic ring stretching vibrations at 1008.7, 735.1, and 592.8 cm^{-1} (Fig. S10). The furanic species on the photocatalyst surface were then extracted using chloroform and analyzed by liquid chromatography-mass spectroscopy (LC-MS). Several components with high molecular weights (Table S4) were observed which are most likely to be furanic oligomers, known as important precursors for producing bio-based polymers or resins [49]. The formation of such oligomers has been observed in past studies [50,51] on the catalysis of furfuryl alcohol and/or fufural conducted in aqueous solution due to the instability of furfuryl alcohol and furfural in the presence of water.
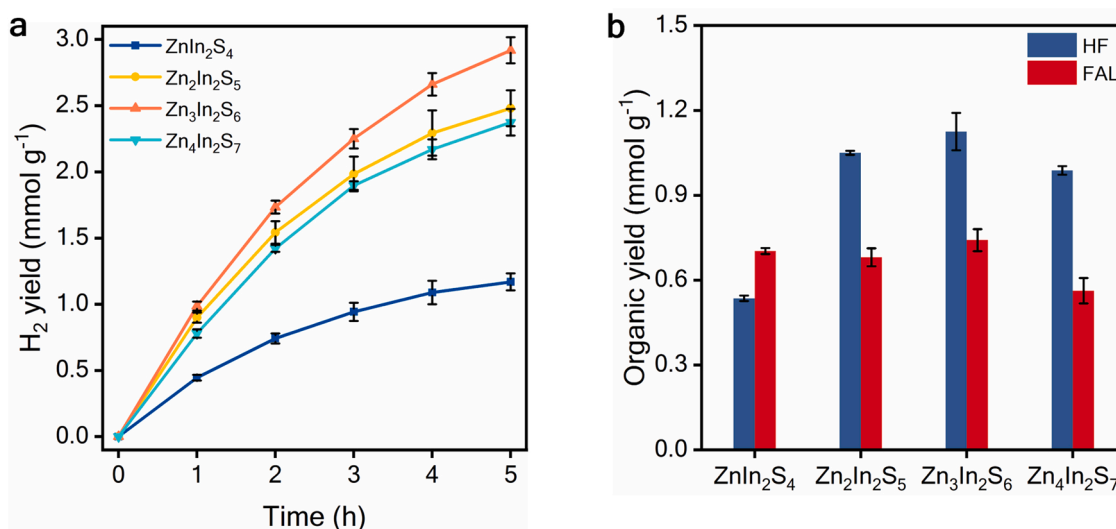

Fig. 4. Furfuryl alcohol (FOL) photoreforming performance by $Zn_xIn_2S_{3+x}$ under visible light illumination. (a) Time-dependent H_2 evolution profiles. (b) Organic product yields after 5 h of reaction.

The intrinsic charge carrier dynamics of $Zn_xIn_2S_{3+x}$ was then investigated using steady-state photoluminescence (PL) spectroscopy with 350 nm laser excitation, chronoamperometry under chopped solar illumination (contains UV portion), and electrochemical impedance spectroscopy (EIS) under dark conditions. PL spectroscopy indicated the x value influenced charge recombination (Fig. 5a). A higher x resulted in $Zn_xIn_2S_{3+x}$ displaying a lower fluorescence intensity, indicating better charge carrier separation. Chronoamperometric I-t plots with chopped illumination (Fig. 5b) show that increasing x from 1 to 4 improves photocurrent density. Collectively, the findings reveal better charge separation and transfer efficiency for $Zn_xIn_2S_{3+x}$ with a higher x. Electrochemical impedance spectroscopy (EIS) indicates that a higher x in $Zn_xIn_2S_{3+x}$ enhances charge transfer, in turn invoking accelerated interfacial electron and hole consumption (Fig. 5c). This is evidenced by the decrease in charge transfer resistance at the photocatalyst/interface (R_p) with increasing x in $Zn_xIn_2S_{3+x}$ (from 10.3 to 5.9 kΩ for x values from 1 to 4 (Table S5)). Overall, the enhanced intrinsic charge carrier dynamics in $Zn_xIn_2S_{3+x}$ at higher x values (independent of the light absorption properties) agrees with the activity obtained under UV irradiation (Fig. S8a,b). The improved carrier dynamics may be correlated to the higher crystallinity, as indicated by the calculated crystallite sizes (Table S6) and larger surface area (Table S2) of $Zn_xIn_2S_{3+x}$ at higher x values.

3.3. Mechanistic study

The majority of alcohol photoreforming studies generate aldehydes or ketones as the oxidation product. In our case, $Zn_xIn_2S_{3+x}$ ($x = 1–4$) facilitates oxidative C-C coupling products. This is verified by the presence of HF in addition to FAL after FOL oxidation. Fig. 6a shows that FOL oxidation involves the activation of its O-H or C-H bond. HF production requires the α-C-H activation of FOL, forming a α-C-centered radical (hydroxyfurfuryl radical (HFF)). HFF radical generation was confirmed by electron paramagnetic resonance (EPR) spectroscopy spin trapping using 5,5-dimethyl-1-pyrroline *N*-oxide (DMPO). The EPR spectra (Fig. 6b) show six characteristic signal peaks corresponding to the DMPO-α-C radical adduct ($α_H = 21.4$ and $α_N = 15.7$) [52] upon light irradiation. HFF radical formation was further verified using liquid chromatography-mass spectrometry (LC-MS) (Fig. S11). The HFF radical is then desorbed from the catalyst surface to undergo C-C coupling in the bulk solution. The presence the FOL hydroxyl group (-OH) generally makes the α-C-H activation step challenging due to the more reactive nature of the O-H bond, to form the furfuryloxy radical (FFO) (Fig. 6a). As suggested by Xie et al., the radical formation mechanism controls preferential C-H or O-H bond activation of the alcohol [16]. Typically, O-H activation favors a stepwise pathway involving proton transfer

followed by electron transfer (PT-ET). In contrast, C-H activation proceeds favorably through a concerted proton-electron transfer (CPET) pathway where the proton and electron transfers occur simultaneously, avoiding the formation of a highly unstable intermediate. Consequently, HF formation on $Zn_xIn_2S_{3+x}$ may be ascribed to the ability of these photocatalysts to facilitate the CPET mechanism during hole transfer. Additionally, subsequent rapid HFF radical desorption is important to prevent oxidation into FAL or CO_2.

The capacity for $Zn_xIn_2S_{3+x}$ to promote the CPET pathway may be linked to the presence of sulfur moieties on the surface as sulfur-based radicals are typically involved in the CPET reaction mechanism [53, 54]. To verify the catalytic role of surface sulfur moieties on $Zn_xIn_2S_{3+x}$, $Zn_3In_2S_6$ alkylation was conducted using 3-(bromopropyl)trimethoxysilane (BPTMOS) (Supplementary Methods) [32,55]. BPTMOS-$Zn_3In_2S_6$ exhibited lower performance and undetectable HF production over 5 h of illumination (Fig. 6c). Treating BPTMOS-$Zn_3In_2S_6$ with NaSH (Supplementary Methods) can regenerate the sulfur active sites [32], increasing performance. HF was detected on NaSH-$Zn_3In_2S_6$ although the yield was lower compared to pristine $Zn_3In_2S_6$ due to incomplete BPTMOS removal from the surface. The ATR-IR spectrum of NaSH-$Zn_3In_2S_6$ in Fig. S12 show that the Si-O vibration band at 1025 cm^{-1} does not completely disappear, indicating that a portion of the BPTMOS remains on the surface following NaSH treatment. The findings demonstrate that sulfur moieties in $Zn_xIn_2S_{3+x}$ contribute to the C-H activation step during FOL photoreforming.

Sulfur anion radical ($S^{-•}$) formation upon illumination was observed using transient absorption spectroscopy (TAS) [56,57]. The $S^{-•}$ species forms when valence band holes become localized on a sulfur atom. The spectra for $ZnIn_2S_4$ and $Zn_3In_2S_6$ (Fig. 6d,e) exhibit extended light absorption in the visible region (>500 nm), corresponding to a $S^{-•}$ species presence. The $S^{-•}$ species absorbs light by transferring an electron into unoccupied levels of $Zn_xIn_2S_{3+x}$ [57]. Similar broad absorption profiles are observed for $Zn_2In_2S_5$ and $Zn_4In_2S_7$ (Fig. S13a,b). The kinetic decay fits in Fig. 6d,e and Figure S13a,b indicate that samples with a higher x boast a longer $S^{-•}$ lifetime. The average $S^{-•}$ lifetimes for $ZnIn_2S_4$, $Zn_2In_2S_5$, $Zn_3In_2S_6$, and $Zn_4In_2S_7$ are 1.05, 1.27, 1.68, and 2.27 ns, respectively.

Understanding the active site assists with establishing the structure-selectivity relationship which links the $Zn_xIn_2S_{3+x}$ photocatalyst characteristics to the reaction mechanism. As seen in Fig. 4b, altering the atomic composition of $Zn_xIn_2S_{3+x}$ delivers higher HF product selectivity. From a structural perspective, a higher x in $Zn_xIn_2S_{3+x}$ provides a higher Zn-S:In-S layer ratio, as was observed from PDF analysis (Fig. 2d,e). Consequently, control studies on pristine In_2S_3 and ZnS photocatalysts may give greater insights on the role of each layer. Fig. S14 shows that FOL photoreforming by In_2S_3 delivers a low H_2 yield (due to severe
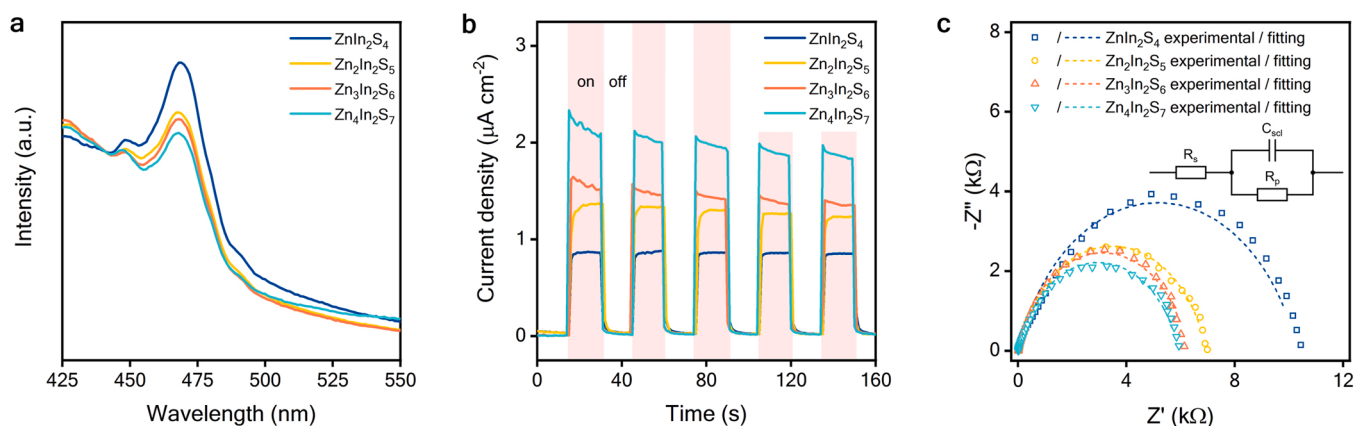
Fig. 5. Carrier dynamics in $Zn_xIn_2S_{3+x}$. (a) Steady-state PL spectra for $Zn_xIn_2S_{3+x}$ obtained using 350 nm laser excitation. (b) Chronoamperometry I-t responses of $Zn_xIn_2S_{3+x}$ under chopped solar simulator illumination at 1.0 V vs RHE. (c) Nyquist plots of $Zn_xIn_2S_{3+x}$ under dark conditions at applied potential of 0.0 V vs RHE. Inset, the equivalent circuit model obtained through curve fittings.
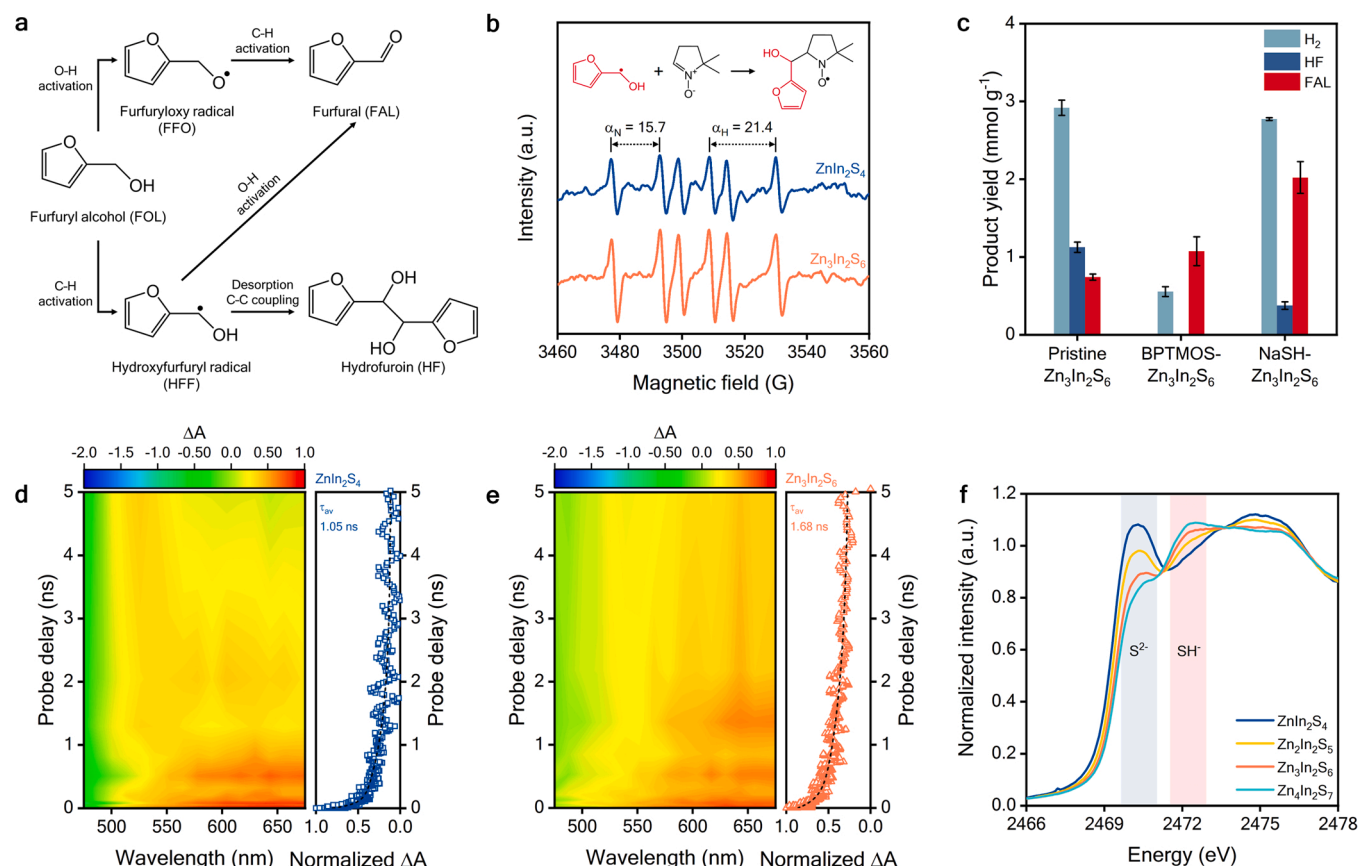
Fig. 6. Reaction mechanism and elucidation of active site for furfuryl alcohol (FOL) photoreforming over $Zn_xIn_2S_{3+x}$. (a) Reaction pathways for FOL photoreforming initiated by O-H activation and C-H activation. (b) EPR spectra of $ZnIn_2S_4$ and $Zn_3In_2S_6$ reaction supernatants after 5 h of UV illumination in the presence of DMPO as a spin-trapping agent. (c) FOL photoreforming performance by BPTMOS-$Zn_3In_2S_6$ and NaSH-$Zn_3In_2S_6$ compared to pristine $Zn_3In_2S_6$ after 5 h of visible light illumination. Contour maps for transient absorption of (d) $ZnIn_2S_4$ and (e) $Zn_3In_2S_6$ to detect sulfur anion radical ($S^{-\bullet}$) under 350 nm photoexcitation and the corresponding kinetic traces showing the decay and kinetic fits of $S^{-\bullet}$ absorption at 600 nm for $ZnIn_2S_4$ and $Zn_3In_2S_6$. (f) S K-edge XAS showing a change in the redox state of S consistent with a change in bonding.

charge recombination) and almost 100% FAL selectivity. Conversely, ZnS produces a higher H_2 yield than In_2S_3 and exhibits a capacity to generate HF. The lower HF selectivity of ZnS compared to $Zn_3In_2S_6$ is ascribed to its highly oxidizing VB that leads to hydroxyl radical formation (non-selective oxidizing species) as suggested by the coumarin test (Fig. S15 and Supplementary Methods). In contrast, the $Zn_3In_2S_6$ VB is not sufficiently energetic to invoke hydroxyl radical generation, rendering it suitable for selectivity tuning. The findings from the control study suggest that the Zn-S layer is the $Zn_xIn_2S_{3+x}$ component contributing to C-H activation of the FOL.

Contribution of the Zn-S layer to C-H activation could be linked to the $Zn_xIn_2S_{3+x}$ VB being composed of hybrid S 3p and Zn 3d orbitals. Consequently, the photogenerated holes may accumulate on the Zn-S layer to form $S^{-\bullet}$ active sites. Further, the Zn atoms binding with S through tetrahedral coordination implies the formation of strong Zn-S bonds, considering that tetrahedral structures commonly offer a covalent feature [58]. It has been shown that the increased covalency enhances electron transfer from Zn and In to S [59]. The S K-edge XAS spectra of $Zn_xIn_2S_{3+x}$ (Fig. 6f) depict a systematic increase in the SH^-:S^{2-} ratio with increasing x, indicating that the sulfur on the Zn-S layer is more oxidized. The distinctive oxidation state of sulfur within $Zn_xIn_2S_{3+x}$ was also observed in S 2p XPS (Fig. S16). The peaks at the S 2p edge of $Zn_xIn_2S_{3+x}$, corresponding to S^{2-} and SH^- species, are shifted to higher binding energies with increasing x (from 161.72 eV and 162.95 eV for $ZnIn_2S_4$ to 162.06 eV and 163.27 for $Zn_4In_2S_7$). In line with the S K-edge XAS spectra, the shift may be ascribed to the increased amounts of more oxidized sulfur species (SH^-) relative to S^{2-} as the Zn-S:

In-S layer ratio in $Zn_xIn_2S_{3+x}$ increases. Consequently, upon light illumination, the photogenerated electrons are attracted to sulfur moieties, particularly in the Zn-S layer. Through electron donation from metal sites, $S^{-\bullet}$ species are stabilized, leading to a prolonged lifetime. The prolonged $S^{-\bullet}$ lifetime over $Zn_xIn_2S_{3+x}$ at higher x values is the factor likely responsible for greater HF selectivity.

The dominant Zn-S layer contribution to C-H activation was validated by density functional theory (DFT) calculations. The catalytic steps for C-H activation of FOL into the HFF radical, including FOL adsorption, α-C-H bond cleavage of adsorbed FOL, and desorption of the generated carbon-centered radical, are calculated on exposed Zn-S and In-S layers for $ZnIn_2S_4$ and $Zn_3In_2S_6$ (Fig. 7a,b). The graphical models in Fig. 7c,d represent the interactions between FOL and Zn-S and In-S surfaces during C-H activation. FOL adsorption via its α-C-H bond is more favorable on the Zn-S layer (−0.45 V and −0.59 V vs RHE) than on the In-S layer (−0.08 V and −0.26 V vs RHE) for both $ZnIn_2S_4$ and $Zn_3In_2S_6$. Further, the calculated adsorption energies indicate FOL adsorption through the α-C-H bond on $Zn_3In_2S_6$ is stronger compared to $ZnIn_2S_4$. Consecutively, the adsorbed FOL undergoes α-C-H bond rupture with an energy barrier (ΔE) of 0.28 V and − 0.26 V vs RHE on Zn-S and In-S layers of $ZnIn_2S_4$ in 0.67 V and 0.69 V vs RHE over Zn-S and In-S layers in $Zn_3In_2S_6$. Beyond the varying energy barriers for α-C-H bond cleavage, all values lie well below the $ZnIn_2S_4$ (1.20 V vs RHE) and $Zn_3In_2S_6$ (1.29 V vs RHE) VBs, suggesting the VBs are sufficiently energetic to drive the cleavage reaction. Consequently, initial FOL adsorption via the α-C-H bond is more likely to be the key step driving C-H activation of the FOL. Additionally, HFF radical desorption
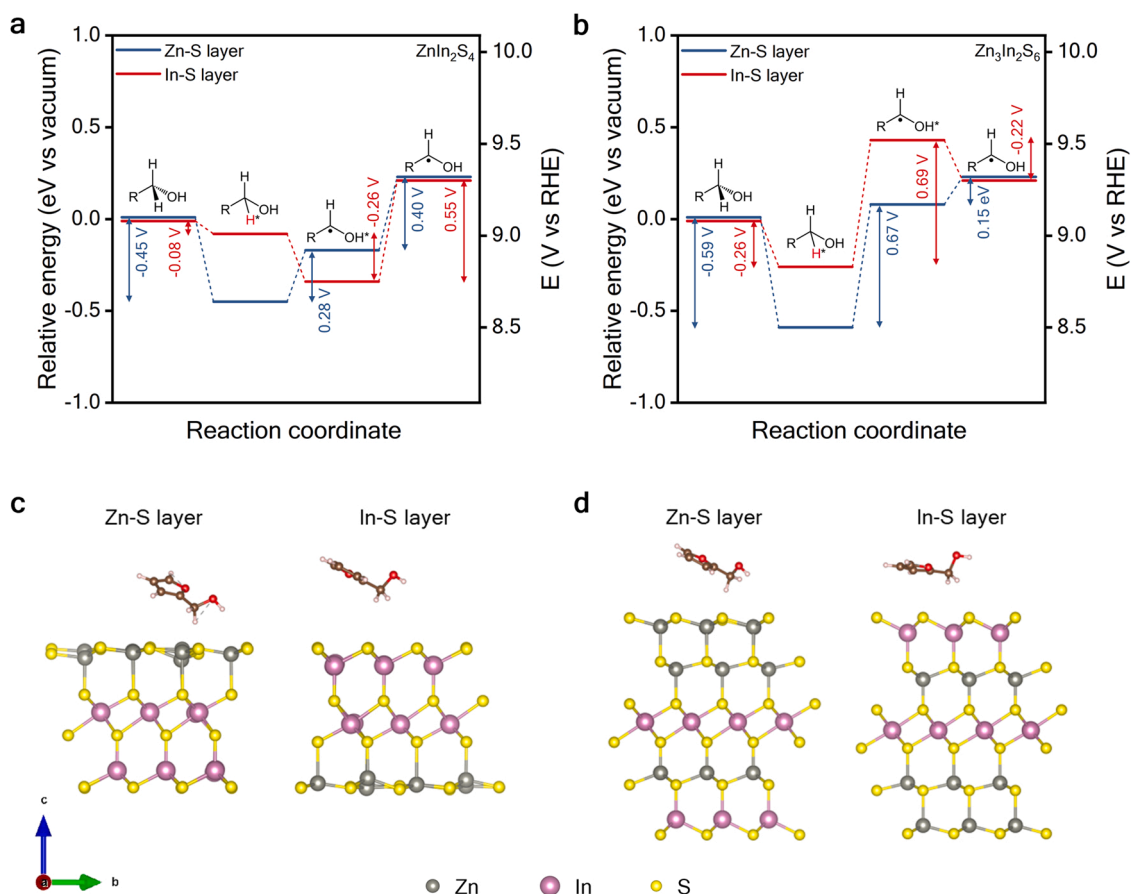
Fig. 7. Density functional theory calculations on C-H activation pathway for furfuryl alcohol (FOL) photoreforming. (a,b) Reaction energy profiles in eV vs vacuum (left *y*-axis) and V vs RHE (right *y*-axis) and (c,d) graphical model representations for C-H activation of FOL on Zn-S and In-S layers over $ZnIn_2S_4$ and $Zn_3In_2S_6$.

on $Zn_3In_2S_6$ (0.15 V and −0.22 V vs RHE for Zn-S and In-S layers, respectively), which is essential to prevent further oxidation, is less energy demanding compared to $ZnIn_2S_4$ (0.40 V and 0.55 V vs RHE for Zn-S and In-S layers, respectively). Collectively, the computational findings confirm the hypothesis that the Zn-S layer of $Zn_xIn_2S_{3+x}$ is more prevalent in promoting C-H activation of FOL, resulting in higher HF selectivity by $Zn_3In_2S_6$ compared to $ZnIn_2S_4$.

3.4. Stability evaluation

As well as activity and selectivity, long-term stability is another critical metric for photoreforming to be practical. The stability of $Zn_3In_2S_6$ was examined by conducting recycling experiments. After a 5 h reaction cycle, $Zn_3In_2S_6$ was collected by centrifuging and thoroughly washed with water and ethyl acetate to remove all impurities. The recovered $Zn_3In_2S_6$ was then reused for a subsequent 5 h reaction cycle. As seen in Fig. S17, the photocatalytic activity in terms of H_2 evolution is relatively stable with a slight decrease. However, the organic product selectivity changes after the first cycle with the FAL yield having increased and the HF yield having decreased.

Post-reaction XRD characterization shows that the bulk structure of $Zn_3In_2S_6$ remains intact after the first cycle (Fig. S18). The stability is ascribed to the increased covalency of $Zn_3In_2S_6$, which improves electron donation from Zn and In to S, in turn stabilizing the generated $S^{-\bullet}$ radicals upon light illumination [59]. This could prolong $S^{-\bullet}$ radical lifetime and prevent the dissolution of sulfur moieties [60]. Nevertheless, the S 2p XPS of spent $Zn_3In_2S_6$ indicates a slight change in sulfur oxidation state after reaction (Fig. S19). The sulfur on the surface was observed to be slightly reduced post reaction, leading to a decrease in the $SH^-:S^{2-}$ ratio as indicated by the peak shifts toward lower binding

energy (from 161.88 eV and 163.08 eV for fresh $Zn_3In_2S_6$ to 161.78 eV and 163.03 eV for spent $Zn_3In_2S_6$). Consequently, this may suppress electron transfer to the $S^{-\bullet}$ active sites upon light illumination, reducing the lifetime of the active sites and leading to lower C-C coupling product selectivity.

4. Conclusion

This study presents visible-light-driven FOL photoreforming on a series of $Zn_xIn_2S_{3+x}$ ($x = 1–4$) photocatalysts to produce H_2 and hydrofuroin via the C-H activation and C-C coupling pathway. An optimum H_2 yield of 2.92 mmol g^{-1} combined with a hydrofuroin yield and selectivity of 1.13 mmol g^{-1} and 43.7%, respectively, was achieved for $Zn_3In_2S_6$ over 5 h of illumination. The optimum $Zn_xIn_2S_{3+x}$ composition is defined by a trade-off between accelerated charge carrier dynamics and lower visible light absorption by the $Zn_xIn_2S_{3+x}$. Importantly, $S^{-\bullet}$ species present in the Zn-S layer of $Zn_xIn_2S_{3+x}$ were found to be the key active sites. Increasing x in $Zn_xIn_2S_{3+x}$ benefitted hydrofuroin selectivity due to a longer lifetime of the $S^{-\bullet}$ active sites, needed for C-H activation of the FOL. Increasing the x value, which corresponds to a higher Zn-S:In-S layer ratio, was found to enhance covalency and electron transfer to the $S^{-\bullet}$ species upon illumination, stabilizing the active sites for C-H activation and delivering a higher C-C coupling product selectivity.

CRediT authorship contribution statement

Denny Gunawan: Conceptualization, Methodology, Investigation, Writing – original draft. **Jodie A. Yuwono:** Formal analysis. **Priyank V. Kumar:** Formal analysis. **Akasha Kaleem:** Investigation. **Michael P.**

Nielsen: Investigation, Validation. **Murad J. Y. Tayebjee:** Investigation, Validation. **Louis Oppong-Antwi:** Investigation. **Haotian Wen:** Investigation. **Inga Kuschnerus:** Investigation. **Shery L. Y. Chang:** Validation, Formal analysis. **Yu Wang:** Investigation, Formal analysis. **Rosalie K. Hocking:** Validation, Formal analysis. **Ting-Shan Chan:** Investigation. **Cui Ying Toe:** Conceptualization, Supervision, Writing – review & editing. **Jason Scott:** Conceptualization, Supervision, Writing – review & editing. **Rose Amal:** Conceptualization, Supervision, Writing – review & editing, Resources.

Declaration of Competing Interest

The authors declare that they have no known competing financial interests or personal relationships that could have appeared to influence the work reported in this paper.

Data Availability

Data will be made available on request.

Author's contribution

D.G., C.Y.T., J.S., and R.A. conceptualized the project. D.G. conducted the bulk of the experiments and characterization. J.A.Y and P.V. K. performed DFT calculations. A.K., M.P.N., and M.J.Y.T. conducted TAS measurements and analysis. L.O.-A. carried out SEM imaging. Y.W. performed XRD measurements in transmission mode and PDF analysis. H.W., I.K., and S.L.Y.C. conducted TEM imaging and analysis. R.K.H and T.-S.C. carried out XAS measurements and analyses. D.G. wrote the original draft of the manuscript. C.Y.T., J.S., and R.A. revised the manuscript. All authors discussed the findings and contributed to completion of the manuscript.

Appendix A. Supporting information

Supplementary data associated with this article can be found in the online version at doi:10.1016/j.apcatb.2023.122880.

References

[1] S. van Renssen, The hydrogen solution? Nat. Clim. Change 10 (2020) 799–801.
[2] D. Gunawan, Unlocking the potential of hydrogen in Indonesia, in: H. Ardiansyah, P. Ekadewi (Eds.), Indonesia Post-Pandemic Outlook: Strategy towards Net-Zero Emissions by 2060 from the Renewables and Carbon-Neutral Energy Perspectives, BRIN Publishing, 2022.
[3] S. Chen, T. Takata, K. Domen, Particulate photocatalysts for overall water splitting, in: Nat. Rev. Mater, 2, 2017. No. 17050.
[4] C.-W. Huang, B.-S. Nguyen, J.C.S. Wu, V.-H. Nguyen, A current perspective for photocatalysis toward the hydrogen production from biomass-derived organic substances and water, Int. J. Hydrog. Energy 45 (2020) 18144–18159.
[5] C.Y. Toe, C. Tsounis, J. Zhang, H. Masood, D. Gunawan, J. Scott, R. Amal, Advancing photoreforming of organics: highlights on photocatalyst and system designs for selective oxidation reactions, Energy Environ. Sci. 14 (2021) 1140–1175.
[6] T. Uekert, C.M. Pichler, T. Schubert, E. Reisner, Solar-driven reforming of solid waste for a sustainable future, Nat. Sustain. 4 (2020) 383–391.
[7] M. Guo, W. Song, J. Buhain, Bioenergy and biofuels: history, status, and perspective, Renew. Sustain. Energy Rev. 42 (2015) 712–725.

[8] P. Zhang, Y.-J. Guo, J. Chen, Y.-R. Zhao, J. Chang, H. Junge, M. Beller, Y. Li, Streamlined hydrogen production from biomass, Nat. Catal. 1 (2018) 332–338.
[9] E. Reisner, When does organic photoredox catalysis meet artificial photosynthesis? Angew. Chem., Int. Ed. 58 (2019) 3656–3657.
[10] M. Chatterjee, T. Ishizaka, H. Kawanami, Accelerated decarbonylation of 5-hydroxymethylfurfural in compressed carbon dioxide: a facile approach, Green. Chem. 20 (2018) 2345–2355.
[11] H. Xie, T. Qi, Y.J. Lyu, J.F. Zhang, Z.B. Si, L.J. Liu, L.F. Zhu, H.Q. Yang, C.W. Hu, Molecular mechanism comparison of decarbonylation with deoxygenation and hydrogenation of 5-hydroxymethylfurfural catalyzed by palladium acetate, Phys. Chem. Chem. Phys. 21 (2019) 3795–3804.
[12] N. An, D. Ainembabazi, C. Reid, K. Samudrala, K. Wilson, A.F. Lee, A. Voutchkova-Kostal, Microwave-assisted decarbonylation of biomass-derived aldehydes using Pd-doped hydrotalcites, ChemSusChem 13 (2020) 312–320.
[13] G. Han, Y.H. Jin, R.A. Burgess, N.E. Dickenson, X.M. Cao, Y. Sun, Visible-light-driven valorization of biomass intermediates integrated with H₂ production catalyzed by ultrathin Ni/CdS nanosheets, J. Am. Chem. Soc. 139 (2017) 15584–15587.
[14] D. Gunawan, C.Y. Toe, P. Kumar, J. Scott, R. Amal, Synergistic cyanamide functionalization and charge-induced activation of nickel/carbon nitride for enhanced selective photoreforming of ethanol, ACS Appl. Mater. Interfaces 13 (2021) 49916–49926.
[15] D. Gunawan, C.Y. Toe, K. Sun, J. Scott, R. Amal, Improved carrier dynamics in nickel/urea-functionalized carbon nitride for ethanol photoreforming, Photochem. Photobiol. Sci. 21 (2022) 2115–2126.
[16] S. Xie, Z. Shen, J. Deng, P. Guo, Q. Zhang, H. Zhang, C. Ma, Z. Jiang, J. Cheng, D. Deng, Y. Wang, Visible light-driven C–H activation and C–C coupling of methanol into ethylene glycol, Nat. Commun. 9 (2018). No. 1181.
[17] H. Zhang, S. Xie, J. Hu, X. Wu, Q. Zhang, J. Cheng, Y. Wang, C–H activations of methanol and ethanol and C–C couplings into diols by zinc-indium-sulfide under visible light, Chem. Commun. 56 (2020) 1776–1779.
[18] T. Mitkina, C. Stanglmair, W. Setzer, M. Gruber, H. Kisch, B. Konig, Visible light mediated homo- and heterocoupling of benzyl alcohols and benzyl amines on polycrystalline cadmium sulfide, Org. Biomol. Chem. 10 (2012) 3556–3561.
[19] Z. Chai, T.T. Zeng, Q. Li, L.Q. Lu, W.J. Xiao, D. Xu, Efficient visible light-driven splitting of alcohols into hydrogen and corresponding carbonyl compounds over a Ni-modified CdS photocatalyst, J. Am. Chem. Soc. 138 (2016) 10128–10131.
[20] N. Luo, T. Hou, S. Liu, B. Zeng, J. Lu, J. Zhang, H. Li, F. Wang, Photocatalytic coproduction of deoxybenzoin and H₂ through tandem redox reactions, ACS Catal. 10 (2019) 762–769.
[21] N. Luo, T. Montini, J. Zhang, P. Fornasiero, E. Fonda, T. Hou, W. Nie, J. Lu, J. Liu, M. Heggen, L. Lin, C. Ma, M. Wang, F. Fan, S. Jin, F. Wang, Visible-light-driven coproduction of diesel precursors and hydrogen from lignocellulose-derived methylfurans, Nat. Energy 4 (2019) 575–584.
[22] Y.-B. Huang, Z. Yang, J.-J. Dai, Q.-X. Guo, Y. Fu, Production of high quality fuels from lignocellulose-derived chemicals: a convenient C–C bond formation of furfural, 5-methylfurfural and aromatic aldehyde, RSC Adv. 2 (2012) 11211–11214.
[23] S.Y. Zhang, F.M. Zhang, Y.Q. Tu, Direct sp³ α-C–H Activation and Functionalization of Alcohol and Ether, Chem. Soc. Rev. 40 (2011) 1937–1949.
[24] J.K. Cheng, T.P. Loh, Copper- and cobalt-catalyzed direct coupling of sp³ α-carbon of alcohols with alkenes and hydroperoxides, J. Am. Chem. Soc. 137 (2015) 42–45.
[25] N. Zhao, M.K. Goetz, J.E. Schneider, J.S. Anderson, Testing the limits of imbalanced CPET reactivity: mechanistic crossover in H-atom abstraction by Co (III)-oxo complexes, J. Am. Chem. Soc. 145 (2023) 5664–5673.
[26] M. Li, W. Guo, R. Jiang, L. Zhao, X. Lu, H. Zhu, D. Fu, H. Shan, Density functional study of ethanol decomposition on Rh(111), J. Phys. Chem. C. 114 (2010) 21493–21503.
[27] H. Lu, J. Zhao, L. Li, L. Gong, J. Zheng, L. Zhang, Z. Wang, J. Zhang, Z. Zhu, Selective oxidation of sacrificial ethanol over TiO₂-based photocatalysts during water splitting, Energy Environ. Sci. 4 (2011) 3384–3388.
[28] P. Yang, J. Zhao, B. Cao, L. Li, Z. Wang, X. Tian, S. Jia, Z. Zhu, Selective photocatalytic C–C coupling of bioethanol into 2,3-butanediol over Pt-decorated hydroxyl-group-tunable TiO₂ photocatalysts, ChemCatChem 7 (2015) 2384–2390.
[29] J. Wang, P. Yang, B. Cao, J. Zhao, Z. Zhu, Photocatalytic carbon–carbon bond formation with concurrent hydrogen evolution on the Pt/TiO₂ nanotube, Appl. Surf. Sci. 325 (2015) 86–90.
[30] Y. Li, J. Cai, M. Hao, Z. Li, Visible light initiated hydrothiolation of alkenes and alkynes over ZnIn₂S₄, Green. Chem. 21 (2019) 2345–2351.
[31] G. Han, X. Liu, Z. Cao, Y. Sun, Photocatalytic pinacol C–C coupling and jet fuel precursor production on ZnIn₂S₄ nanosheets, ACS Catal. 10 (2020) 9346–9355.
[32] J. Lin, X. Wu, S. Xie, L. Chen, Q. Zhang, W. Deng, Y. Wang, Visible-light-driven cleavage of C–O linkage for lignin valorization to functionalized aromatics, ChemSusChem 12 (2019) 5023–5031.
[33] C.L. Farrow, P. Juhas, J.W. Liu, D. Bryndin, E.S. Bozin, J. Bloch, T. Proffen, S. J. Billinge, PDFfit2 and PDFgui: computer programs for studying nanostructure in crystals, J. Phys. Condens. Matter 19 (2007), 335219.
[34] M. Abdullah, G.K.-C. Low, R.W. Matthews, Effects of common inorganic anions on rates of photocatalytic oxidation of organic carbon over illuminated titanium dioxide, J. Phys. Chem. 94 (1990) 6820–6825.
[35] G. Kresse, J. Furthmüller, Efficiency of ab-initio total energy calculations for metals and semiconductors using a plane-wave basis set, Comput. Mater. Sci. 6 (1996) 15–50.
[36] G. Kresse, J. Hafner, Efficient iterative schemes for ab initio total-energy calculations using a plane-wave basis set, Phys. Rev. B 54 (1996) 11169–11186.

[37] P.E. Blöchl, Projector augmented-wave method, Phys. Rev. B Condens. Matter 50 (1994) 17953–17979.

[38] G. Kresse, D. Joubert, From ultrasoft pseudopotentials to the projector augmented-wave method, Phys. Rev. B 59 (1999) 1758–1775.

[39] J.P. Perdew, K. Burke, E. Matthias, Generalized gradient approximation made simple, Phys. Rev. Lett. 77 (1996) 3865–3868.

[40] S. Grimme, J. Antony, S. Ehrlich, H. Krieg, A consistent and accurate ab initio parametrization of density functional dispersion correction (DFT-D) for the 94 elements H-Pu, J. Chem. Phys. 132 (2010).

[41] F. Fang, L. Chen, Y.B. Chen, L.M. Wu, Synthesis and photocatalysis of $ZnIn_2S_4$ nano/micropeony, J. Phys. Chem. C 114 (2010) 2393–2397.

[42] X. Jiao, Z. Chen, X. Li, Y. Sun, S. Gao, W. Yan, C. Wang, Q. Zhang, Y. Lin, Y. Luo, Y. Xie, Defect-mediated electron-hole separation in one-unit-cell $ZnIn_2S_4$ layers for boosted solar-driven CO_2 reduction, J. Am. Chem. Soc. 139 (2017) 7586–7594.

[43] K.-W. Cheng, Y.-H. Cheng, M.-S. Fan, Photoelectrochemical study of $ZnIn_2Se_4$ electrodes fabricated using selenization of RF magnetron sputtered Zn–In metal precursors, Int. J. Hydrog. Energy 37 (2012) 13763–13769.

[44] I. Tsuji, H. Kato, H. Kobayashi, A. Kudo, Photocatalytic H_2 evolution reaction from aqueous solutions over band structure-controlled $(AgIn)_xZn_{2(1-x)}S_2$ solid solution photocatalysts with visible-light response and their surface nanostructures, J. Am. Chem. Soc. 126 (2004) 13406–13413.

[45] S. Shen, L. Zhao, L. Guo, $Zn_mIn_2S_{3+m}$ (m=1–5, integer): a new series of visible-light-driven photocatalysts for splitting water to hydrogen, Int. J. Hydrog. Energy 35 (2010) 10148–10154.

[46] Y. Wu, H. Wang, W. Tu, S. Wu, J.W. Chew, Effects of composition faults in ternary metal chalcogenides (Zn_xIn2S_{3+x}, x = 1–5) layered crystals for visible-light-driven catalytic hydrogen generation and carbon dioxide reduction, Appl. Catal., B 256 (2019).

[47] X. Wu, Y.H. Ng, W.H. Saputera, X. Wen, Y. Du, S.X. Dou, R. Amal, J. Scott, The dependence of Bi_2MoO_6 photocatalytic water oxidation capability on crystal facet engineering, ChemPhotoChem 3 (2019) 1246–1253.

[48] D.E. Scaife, Oxide semiconductors in photoelectrochemical conversion of solar energy, Sol. Energy 25 (1980) 41–54.

[49] Y. Lee, E.E. Kwon, J. Lee, Polymers derived from hemicellulosic parts of lignocellulosic biomass, Rev. Environ. Sci. Biotechnol. 18 (2019) 317–334.

[50] X.H. Chadderdon, D.J. Chadderdon, J.E. Matthiesen, Y. Qiu, J.M. Carraher, J. P. Tessonnier, W. Li, Mechanisms of furfural reduction on metal electrodes: distinguishing pathways for selective hydrogenation of bioderived oxygenates, J. Am. Chem. Soc. 139 (2017) 14120–14128.

[51] J. Anibal, B. Xu, Electroreductive C–C coupling of furfural and benzaldehyde on Cu and Pb surfaces, ACS Catal. 10 (2020) 11643–11653.

[52] M.-Y. Qi, Y.-H. Li, M. Anpo, Z.-R. Tang, Y.-J. Xu, Efficient photoredox-mediated C–C coupling organic synthesis and hydrogen production over engineered semiconductor quantum dots, ACS Catal. 10 (2020) 14327–14335.

[53] A. Talla, B. Driessen, N.J.W. Straathof, L.-G. Milroy, L. Brunsveld, V. Hessel, T. Noël, Metal-free photocatalytic aerobic oxidation of thiols to disulfides in batch and continuous-flow, Adv. Synth. Catal. 357 (2015) 2180–2186.

[54] R.S. Glass, Sulfur radicals and their application, Top. Curr. Chem. 376 (2018) 22.

[55] M. Hopfner, H. Weiss, D. Meissner, F.W. Heinemann, H. Kisch, Semiconductor photocatalysis type B: synthesis of unsaturated alpha-amino esters from imines and olefins photocatalyzed by silica-supported cadmium sulfide, Photochem. Photobiol. Sci. 1 (2002) 696–703.

[56] P.V. Kamat, N.M. Dimitrijevic, R.W. Fessenden, Photoelectrochemistry in particulate systems. 6. Electron-transfer reactions of small cadmium sulfide colloids in acetonitrile, J. Phys. Chem. 91 (1987) 396–401.

[57] J.A. Christians, P.V. Kamat, Trap and tansfer. Two-step hole injection across the Sb_2S_3/CuSCN interface in solid-state solar cells, ACS Nano 7 (2013) 7967–7974.

[58] F. Aymerich, F. Meloni, G. Mula, Electronic properties of the layer compound $ZnIn_2S_4$, Phys. B 99 (1980) 314–317.

[59] L.P. Chi, Z.Z. Niu, X.L. Zhang, P.P. Yang, J. Liao, F.Y. Gao, Z.Z. Wu, K.B. Tang, M. R. Gao, Stabilizing indium sulfide for CO_2 electroreduction to formate at high rate by zinc incorporation, Nat. Commun. 12 (2021) 5835.

[60] T. Lange, S. Reichenberger, S. Ristig, M. Rohe, J. Strunk, S. Barcikowski, R. Schlögl, Zinc sulfide for photocatalysis: white angel or black sheep? Prog. Mater. Sci. 124 (2022).